



Buckling of a thin elastic rod inside a horizontal cylindrical constraint



J.T. Miller^{a,1}, T. Su^b, J. Pabon^b, N. Wicks^b, K. Bertoldi^{c,d}, P.M. Reis^{a,e,*}

^a Department of Civil and Environmental Engineering, Massachusetts Institute of Technology, Cambridge, MA 02139, USA

^b Schlumberger-Doll Research, One Hampshire Street, Cambridge, MA 02139, USA

^c School of Engineering and Applied Sciences, Harvard University, Cambridge, MA 02138, USA

^d Kavli Institute for Bionano Science and Technology, Harvard University, Cambridge, MA 02138, USA

^e Department Mechanical Engineering, Massachusetts Institute of Technology, Cambridge, MA 02139, USA

ARTICLE INFO

Article history:

Received 20 January 2015

Accepted 4 March 2015

Available online 15 March 2015

Keywords:

Thin elastic rods

Buckling

Geometric nonlinearities

ABSTRACT

We present results from an experimental and numerical investigation on the compression, and consequent buckling, of a slender rod constrained inside a horizontal cylinder. An experimental model system is developed to systematically study the sequence of instabilities from straight-to-sinusoidal and sinusoidal-to-helical configurations. We quantify the associated buckling loads as a function of the radial clearance between the rod and cylindrical constraint. These results are compared to existing theoretical predictions. While good agreement is obtained for large values of the radial clearance, significant deviations are found when the geometric imperfections of the setup are comparable to the radial clearance. Due to this imperfection sensitivity, the critical buckling loads can be reduced significantly by up to a factor of three. The findings from this model system can be applied to practical applications across a range of length scales due to the geometric (rather than material) nonlinearities involved in the deformations of rods.

© 2015 Elsevier Ltd. All rights reserved.

1. Introduction

Buckling of slender rodlike structures under lateral confinement can lead to complex geometric nonlinearities and is ubiquitous in both natural and engineered settings, across a wide range of length scales. Examples include DNA packings inside viral capsules [1], silicon nanowires attached to stretchable substrates [2], jamming of nanorods confined inside a channel [3], coiling of rods onto rigid surfaces [4,5] plant roots penetrating into substrates that have

a graded stiffness [6] and kilometer-long pipes inside of a borehole in oil well operations [7,8].

In the context of drilling, the buckling of a rod inside a vertical cylinder was first investigated by Lubinski et al. [9,7], using equilibrium methods and neglecting the effect of friction. For the case of an inclined, or horizontal, cylindrical constraint, past a first critical load, P_s , the rod takes on a sinusoidal configuration, with a well defined wavelength, λ_c^s . Lateral deflections of the buckled rod are penalized by the combined effect of elastic and gravitational potential energies, which makes higher buckling modes more energetically favorable than the first mode. Following energy methods, expressions for P_s and λ_c^s were derived by Paslay and Bogey [8] and Dawson and Paslay [10], respectively. Further compression past a second critical load, P_h , results in the rod transitioning into a helical configuration. Chen et al. [11] obtained an expression for

* Corresponding author at: Department of Civil and Environmental Engineering, Massachusetts Institute of Technology, Cambridge, MA 02139, USA.

E-mail address: preis@mit.edu (P.M. Reis).

¹ Now a Research Associate with Schlumberger-Doll Research.

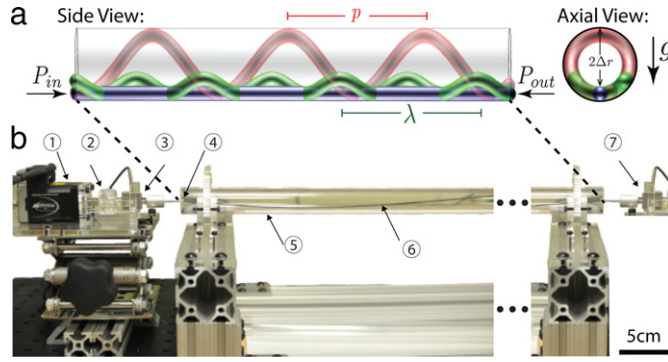


Fig. 1. Experimental apparatus. (a) Schematic diagram of the configurations of the Nitinol rod inside the horizontal constraining pipe for increasing load. The initially straight rod (blue) first buckles into a sinusoidal configuration (green) with wavelength λ , and then into a helical configuration (red) with pitch length p . The axial view (right) illustrates the radial clearance, $2\Delta r$, between the rod and the pipe. (b) Side view photograph of the experiment: (1) linear actuator, (2) load cells, (3) aluminum pins, (4) acrylic pipe, (5) Nitinol rod, (6) aluminum frame. The Nitinol rod and the acrylic pipe are both 3.095 m long. For clarity, the photograph has been truncated (marked with ...). (For interpretation of the references to color in this figure legend, the reader is referred to the web version of this article.)

P_h that is, to date, still widely used, even if there is some disagreement in the literature [12–15]. Within this helical regime, Lubinski and Althouse [7] proposed a load–pitch relationship and Mitchell [16] established that the normal contact force between the helically buckled rod and the cylindrical constraint is quadratically proportional to the applied loads at the end boundaries of the rod. These main results have also been ported to the application of coiled tubing operations, wherein a pipe is injected into a horizontal wellbore, with similar, albeit heterogeneous, behavior observed. For more details on this application, see [17].

The preceding studies were performed under the simplifying assumptions of frictionless rod–constraint interaction and perfect contact along its entire length. The role of frictional drag on the end loads has been considered by Wu and Juvkam-Wold [13], and the effect of end torque has also been investigated [14,12,18]. Gao and Miska [19,20] later obtained expressions for the critical sinusoidal and helical loads for the case when lateral friction between the rod and constraint is considered. More recently, Chen et al. [21–23] have taken into account the contact loss between the rod and the constraint. Beyond perfectly straight constraints, the buckling of a rod inside a cylinder whose long axis has a constant curvature has also been investigated [24,25]. Many studies include experimental confirmation of theoretical results [13,25–28] for limited combinations of pipe and constraint diameters. However, to date, there has been no systematic study that combines experiments and numerics to explore how this behavior depends on geometric and material parameters, as well as test and validate existing theories, in detail.

Here, we perform a combined experimental and numerical investigation of the buckling of a rod inside a cylinder, over a wide range of radial clearances between the rod and the constraint. Our precision experiments are performed on a benchtop-scale apparatus, which allows for the accurate control of the underlying parameters and a detailed measurement of the mechanical response. The numerical simulations use the Kirchhoff rod model to solve for the dynamics of the cylindrically constrained rod. A direct comparison between experiments and simulations, with no fitting parameters, yields good agreement

in the force–displacement phenomenology and the frictional drag characteristics, as well as on how the critical loads for sinusoidal and helical buckling depend on radial clearance. We also find that geometric imperfections of the constraint, *i.e.* deviations from a perfectly straight pipe, have significant effects on the critical loads compared to theoretical predictions, and that they manifest differently in the cases of sinusoidal and helical buckling.

Our paper is organized as follows. In Section 2, we introduce the experimental apparatus and the corresponding computational framework in Section 3. The combined experimental and numerical results are presented in Section 4, focusing on representative load–displacement curves (Section 4.1), the dependence of the critical loads on the governing parameters (Section 4.2) and the effect of imperfection (Section 4.3). Finally, in Section 5 we summarize the main results of the paper, present conclusions and provide a perspective for future work.

2. Experimental setup

In Fig. 1, we present a schematic and photograph of our apparatus. The experiments consisted of compressing a Nitinol rod inside an acrylic pipe (3.095 m long). The pipe was set horizontal and mounted onto a stiff aluminum frame by five acrylic clamps that were spaced at 75 cm intervals. Seven different pipes with inner diameters in the range $D_i = 3\text{--}19$ mm were used. Two Nitinol rods were used with diameter $d = 2r = \{1.14, 1.60\}$ mm and Young's moduli $E = \{68.67 \pm 0.27, 68.05 \pm 0.15\}$ GPa, respectively. For both of these rods, the volumetric density was $\rho = 6539 \pm 82$ kg/m³, and the static and dynamic coefficients of friction (between the outer surface of the Nitinol rod and the inner surface of the acrylic constraining pipe) were $\mu_s = 0.45 \pm 0.07$ and $\mu_d = 0.30 \pm 0.03$, respectively. Both μ_s and μ_d were measured in the axial direction of the rod/pipe and we assumed that the lateral coefficient of friction was equal to the axial counterpart. The combination of the various acrylic pipes and rods resulted in 14 experimental radial clearances, Δr , which refers to the relative confinement of the rod, as shown in Fig. 1(a).

The rod was compressed from one of its ends, and along the axial direction of the constraining pipe, by a worm gear linear actuator controlled by a stepper motor, that provided horizontal travel with a maximum displacement of 2 cm. The extremity of the rod near the actuator is referred to as the *input* end and the other as the *output* (dead) end. At the input end, a load cell (22.2 N-capacity) was mounted between the linear actuator and an aluminum pin that held the Nitinol rod concentrically within the constraining pipe. The rods used were sufficiently long for the majority of their length to rest along the bottom of the constraint at the beginning of a test. The load cell measured the input load, P_{in} . The aluminum pin was machined to allow the end of the Nitinol rod to rotate with three degrees of freedom while imposing axial position by inserting the rod end into a small (0.3 mm-deep, 1.6 mm-diameter) recess on the pin face. At the output end, the rod was held by an identical aluminum pin which attached to the rigid frame via another load cell, that allowed for measuring the output load, P_{out} .

Each experimental run consisted of first positioning the Nitinol rod inside the horizontal pipe and placing its ends into the two pin recesses. At this stage, we ensured that P_{in} and P_{out} were balanced to within 0.4 N of each other. Loading (compression) was then accomplished by quasistatically increasing the position of the input end in steps of 10 μ m, while recording both P_{in} and P_{out} . Note that, during a run, P_{out} was always less than P_{in} due to frictional losses between the rod and the pipe. Both the stepper motor control and the data acquisition were computer controlled using LabView. A run was stopped when either the maximum travel (2 cm) of the input end was reached or when the reaction load on either end reached 90% of the capacity of the load cells. At the end of a run, the system was unloaded by reverse-stepping the linear actuator back to the original position. An experimental test for specific values of the control parameters (e.g. rod or pipe diameters) comprised five identical runs to confirm reproducibility. At the end of each test, the Nitinol rod and/or the acrylic pipe were changed for a new geometry, and both the rod and pipe were cleaned with a cotton cloth prior to performing a new test.

3. Numerical framework

Our simulations use the shearable and extensible Kirchhoff rod model [29–33] to describe the elastic rod within the cylindrical constraint. In this framework, the rod is characterized by both its center line position $\mathbf{r}(s, t)$, and a material triad $\hat{\mathbf{d}}_i(s, t)$ ($i = 1, 2, 3$) attached to every cross section that follows the twist along the rod. The arc length of the undeformed rod is s (with $s = 0$ at the input end, where the rod is compressed), t is time, $\hat{\mathbf{d}}_1$ and $\hat{\mathbf{d}}_2$ lie on the cross section plane whose unit normal is $\hat{\mathbf{d}}_3$ (for further details on the Kirchhoff rod formulation, see [34]). The four remaining unknowns include the tensile and shear strains, $\boldsymbol{\gamma}(s, t)$ (with $\gamma_3 = \boldsymbol{\gamma} \cdot \hat{\mathbf{d}}_3$ representing tensile strain), and the bending and twisting strains, $\boldsymbol{\kappa}(s, t)$ (with $\kappa_3 = \boldsymbol{\kappa} \cdot \hat{\mathbf{d}}_3$ denoting the twisting strain). Note that the shear and extensional strains $\boldsymbol{\gamma} = \partial \mathbf{r} / \partial s - \hat{\mathbf{d}}_3$ can be non-zero since the

rod is not assumed to be inextensible nor unshearable. In other words, $\hat{\mathbf{d}}_3$ is not required to be tangent to the centerline of the rod.

Under these assumptions, the governing equations of the rod are the conservation of linear and angular momentum, respectively,

$$\frac{\partial(\rho \mathbf{v})}{\partial t} = \frac{\partial(\mathbf{B}\boldsymbol{\gamma})}{\partial s} + \mathbf{F}_{ext}, \quad (1)$$

$$\frac{\partial(\mathbf{I}\boldsymbol{\omega})}{\partial t} = \frac{\partial(\mathbf{G}\boldsymbol{\kappa})}{\partial s} + \left(\boldsymbol{\gamma} + \hat{\mathbf{d}}_3\right) \times (\mathbf{B}\boldsymbol{\gamma}) + \mathbf{Q}_{ext}, \quad (2)$$

where ρ is the density, $\mathbf{v} = \partial \mathbf{r} / \partial t$ is the velocity, \mathbf{I} is the mass moment of inertia tensor, $\boldsymbol{\omega}$ is the angular velocity of the material triad, $\mathbf{B} = GA\hat{\mathbf{d}}_1\hat{\mathbf{d}}_1 + GA\hat{\mathbf{d}}_2\hat{\mathbf{d}}_2 + EA\hat{\mathbf{d}}_3\hat{\mathbf{d}}_3$, so that $\mathbf{B}\boldsymbol{\gamma}$ represents the internal elastic forces; and $\mathbf{G} = EI\hat{\mathbf{d}}_1\hat{\mathbf{d}}_1 + EI\hat{\mathbf{d}}_2\hat{\mathbf{d}}_2 + GJ\hat{\mathbf{d}}_3\hat{\mathbf{d}}_3$, so that $\mathbf{G}\boldsymbol{\kappa}$ represents the internal elastic moments and torques. Here, E, G, A, I , and J are Young's modulus, shear modulus, cross-sectional area, second moment of inertia, and polar moment of inertia, respectively. Finally, \mathbf{F}_{ext} and \mathbf{Q}_{ext} are the external applied forces and moment per unit rod reference length.

In order to apply the above Kirchhoff model to our case of a rod compressed inside a cylindrical constraint, we need to consider the external forces and moments, namely: (i) gravity, (ii) normal contact force and (iii) friction exerted by the cylindrical wall onto the rod. First, the gravitational force per unit length is

$$\mathbf{F}_{gravity} = \rho g A \hat{\mathbf{e}}_z, \quad (3)$$

where ρ is the volumetric density of the rod, g is the acceleration due to gravity and $\hat{\mathbf{e}}_z$ points vertically downwards.

Second, when rod-channel contact occurs, the normal contact force is in the radial direction of the constraint. It consists of an elastic and an inelastic part $\mathbf{F}_{contact} = -(N_{elastic} + N_{inelastic})\hat{\mathbf{n}}$. The magnitude of the elastic contact force per unit length $N_{elastic}$ can be determined by the radial penetration, δ , of the rod into the constraint (if penetration occurs):

$$\delta = BN_{elastic} \left[\frac{2}{3} + \log \left(\frac{\Delta r}{BN_{elastic}} \right) \right] + \frac{N_{elastic}}{k}, \quad (4)$$

where B and k are two constants computed using the geometry of the rod and the constraint, Δr is the radial clearance of the rod inside the constraint. The expression for this penetration comes from the Hertzian contact between two cylindrical bodies plus the inherent compliance of the two cross-sections. The magnitude of the inelastic part of the contact force, $N_{inelastic}$, is determined by the radial velocity of the rod \mathbf{v}_n at the point of contact:

$$N_{inelastic} = C \mathbf{v}_n, \quad (5)$$

where C is a constant computed using the coefficient of restitution of the contact. Both the elastic and inelastic parts of the contact force act normal to the inner surface of the constraining pipe, if and only if, it is in contact with the pipe wall. More information on the contact model can be found in Refs. [35–38].

Finally, friction is assumed to obey Coulomb law

$$\mathbf{F}_{friction} \leq -\mu |\mathbf{F}_{contact}| \frac{\mathbf{v}_{contact}}{|\mathbf{v}_{contact}|}, \quad (6)$$

where μ is the friction coefficient and $\mathbf{v}_{\text{contact}}$ is the portion of the velocity vector of the contact point that is tangent to the cylindrical constraint (perpendicular to $\hat{\mathbf{n}}$). It is important to note that because friction acts on the surface of the rod, instead of at its center, the moment, $\mathbf{Q}_{\text{ext}} = r\hat{\mathbf{n}} \times \mathbf{F}_{\text{friction}}$, emerges and must also be taken into account (no other moments are considered). We also distinguish between static and dynamic friction coefficients, both of which were measured in the experiments. We realize that the Coulomb friction law introduces hard non-linear behavior at the onset of movement and at the onset of stopping. This has been carefully addressed at every integration time step by first solving the equations of motion in the absence of friction. Then, based on the predicted result without friction and predetermined limits on friction effects over the time step, we introduce the appropriate amount of change due to friction, so that the result is consistent with the physical expectation.

Our simulations solve for the dynamics of the cylindrically constrained Kirchhoff rod model described above, following an approach similar to that previously applied to study the transient dynamics of drillstrings [36–38]. First, the rod is discretized into segments, each of which is characterized by its position and orientation. At each computational time step, the extension, bending, twisting, and shear strains are computed for each segment using the current position and orientation of the rod following the Kirchhoff model described above. The stresses along the rod are then computed from these strains, making use of the constitutive law, for which we assume an isotropic linear elastic material. The validity of this assumption is supported by the fact that, given the slenderness of the rod, the material strains remain small throughout the loading process, despite the large displacements and rotations of the rod. From these stresses, we calculate the internal forces acting between neighboring segments that, combined with the external forces (e.g., gravity and the normal/tangential frictional contact forces with constraint), yield the total force acting on each segment. The acceleration of the segments can then be determined and, subsequently, the positions updated for the next numerical time step using a Newton–Raphson iteration scheme. The time step ($dt = 1.6 \times 10^{-6}$ s) and segment length ($L = 2.54$ mm) were selected based on a convergence analysis.

4. Results

Having introduced our methodology and approach, we proceed with the presentation of our combined experimental and numerical results and a detailed comparison to existing theories. We focus on load–displacement curves (Section 4.1), measure the critical buckling loads (Section 4.2) and evaluate the importance of geometric imperfections in the buckling process of our system (Section 4.3).

4.1. Load–displacement curves

In Fig. 2(a) we present a representative reaction load versus displacement curve for a Nitinol rod ($d = 1.14$ mm) that is compressed axially inside a pipe with $ID = 9.4$ mm

($\Delta r = 4.1$) for both experiments (solid symbols) and simulations (hollow symbols). The reaction loads at the *input* end, P_{in} (circles), and *output* end, P_{out} (triangles), of the apparatus are recorded by the load cells on both extremities (see Section 2). The two signals are similar up to $\delta \approx 2.5$ mm in the experimental data and $\delta \approx 2$ mm in the simulation, beyond which there is a growing *load loss*, $\Delta P = P_{\text{in}} - P_{\text{out}}$. This is due to the increasing *frictional drag* between the rod and the surface of the constraining pipe. In the simulations, there is a large peak just prior to sinusoidal buckling, which we do not observe consistently in the experiments. We attribute this difference to the fact that, in the simulations, the rod is perfectly straight (with its ends laying on the bottom of the constraining pipe), which results in an overshooting of the critical buckling force; a common issue in structural stability algorithms [39].

The region inside the dashed box of Fig. 2(a) is a zoom of Fig. 2(b), in the range $0 < \delta [\text{m}] < 0.004$. The rod is initially straight and exhibits a reaction load that is both linear and stiff until the first (of two) buckling transitions into the sinusoidal configuration at δ_s . After this point, there is a dramatic drop in the slope of the P – δ curve. During this sinusoidal regime, P_{in} and P_{out} remain similar indicating that there is a nearly full load transfer from the input to the output end. As the rod is compressed further, there is a sudden drop in both P_{in} and P_{out} at δ_h , when the rod transitions from a sinusoidal into a helical configuration (observed as the rod touches the top of the pipe) and momentarily loses contact with the constraining cylinder during the mode change. Beyond this point, we find synchronized drops in P_{in} and P_{out} that corresponds to the formation of new helical pitches. The helical configuration of the rod, rather than being a uniform helix, contains a number of regions where chirality inverts (known as perversions in the literature of rods [40]), presumably due to the friction-induced frustration of torsion along the length of the pipe. Between δ_s and δ_h in the simulation data, we also observe high variation in both P_{in} and P_{out} , which we attribute to the propagation of elastic axial waves in the simulation, which does not include material damping.

The growing separation between P_{in} and P_{out} (Fig. 2(a)) in the helical regime, past δ_h , is due to the increase in the normal contact force with the constraint. This causes an increase in frictional drag, which, when integrated over the full length of the rod makes up for ΔP . In Fig. 2(c), we plot ΔP versus δ for experiments (solid circles) and simulations (hollow circles). We note that this plot is different from previous work [13,26,27], which has plotted ΔP as a function of P_{in} . For imposed displacements below $\delta < \delta_h$, the load loss is approximately constant and equal to the sliding friction resistance; $\Delta P \approx \mu_d mg$, where m is the total mass of the rod. Past helical initiation, $\delta > \delta_h$, we find that $\Delta P \sim \delta^2$. This power-law behavior is robust across all experimental tests with other values of d and Δr . The quadratic dependence between end displacement and normal contact force (which, when combined with friction, yields ΔP) has been predicted [7,16], *even though* the theoretical work assumed frictionless interactions between the rod and the constraint. The $\Delta P \sim W_n \sim \delta^2$ behavior can therefore be attributed to the nonlinear geometry of the configuration, and the varying axial load in the rod (due to frictional drag) does not affect the functional relationship between displacement and normal contact force.

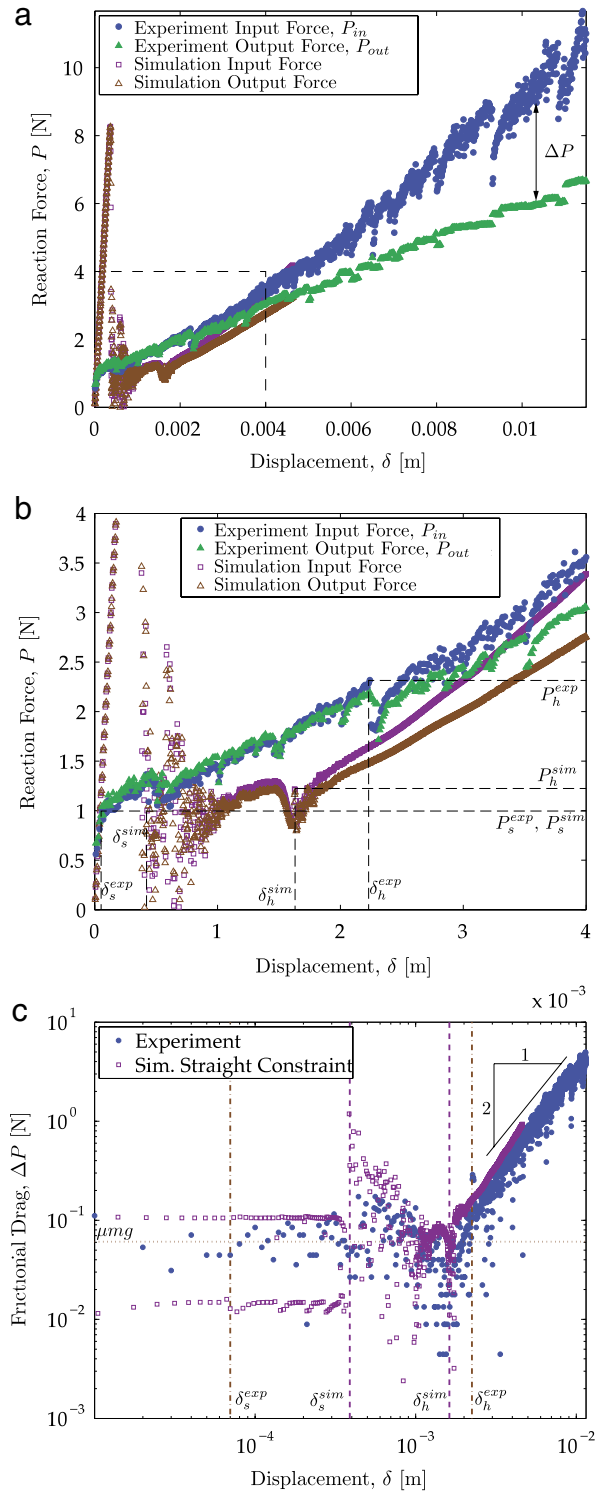


Fig. 2. (a) Reaction force for experiments (solid symbols) and simulations (hollow symbols) at the input end, P_{in} (circles), and output end, P_{out} (triangles), as a function of imposed displacement, δ , for a representative test ($ID = 9.4$ mm, $d = 1.14$ mm, $\Delta r = 4.1$ mm). (b) Zoom of region inside the dashed box in (a), over the range $0 < \delta < 0.004$. The critical indentations, δ_s and δ_h , and critical loads, P_s and P_h , for the transitions between the straight-to-sinusoidal and sinusoidal-to-helical configurations, respectively, are marked in the plot for the experimental values. (c) Load loss between input and output ends, $\Delta P = P_{in} - P_{out}$, as a function of imposed displacement, δ , for experiments (solid symbols) and simulations (hollow symbols).

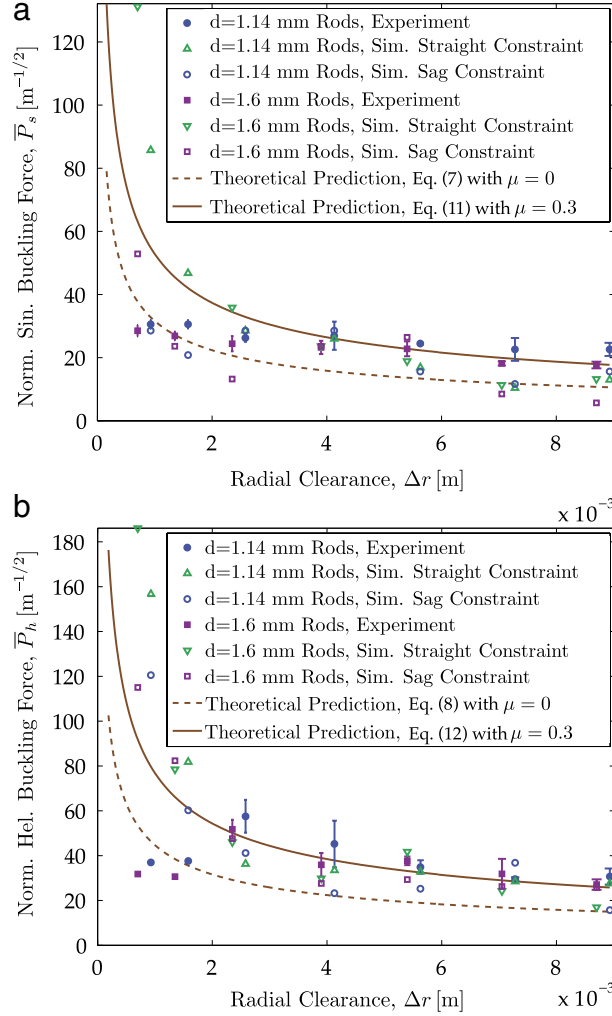


Fig. 3. Normalized critical (a) sinusoidal and (b) helical buckling loads (\bar{P}_s and \bar{P}_h , respectively) as a function of Δr . Experimental values are the mean of five runs with error bars representing the standard deviation. These values are compared to theoretical predictions from the literature for the case of frictionless (dashed line) and frictional (solid line) interactions between the rod and constraint [8,11].

4.2. Critical loads for sinusoidal and helical buckling

We now turn to studying the loads at which the constrained rod configurations transition from straight to sinusoidal, P_s , and from sinusoidal to helical, P_h . In the previous section, we indicated how critical loads were identified by critical points on the P - δ curves. Motivated by results from the recent literature [8,11,19,20] (discussed in more detail below), loads are normalized by $2\sqrt{EIw}$ (and denoted by an overbar, e.g., $\bar{P}_s = P_s / (2\sqrt{EIw})$), where EI is the bending stiffness of the rod (I is the second moment of inertia) and $w = \rho g \pi r^2$ is its weight per unit length.

In Fig. 3(a), (b), we plot the normalized sinusoidal and helical buckling loads, \bar{P}_s and \bar{P}_h , respectively, obtained from experiments (solid symbols) and simulations (hollow symbols), as a function of Δr , for the two rods with $d = \{1.14, 1.6\}$ mm. We also compare the experimental data with two different theoretical predictions from the existing literature [8,11]. The simulation results are further subdivided into results with perfectly axially straight

constraining cylinders (hollow circles and squares) and those with geometric imperfections of the constraint that match the experimentally measured values (hollow triangles). The nature of these imperfections will be discussed in detail in Section 4.3.

The first theory (dashed lines in Fig. 3(a), (b)) [8,11] assumes a frictionless rod–constraint interaction and provides the following predictions for the normalized sinusoidal and helical buckling loads, respectively,

$$\bar{P}_s(\mu = 0) = \frac{P_s}{2\sqrt{EIw}} = \frac{1}{\sqrt{\Delta r}}, \quad (7)$$

$$\bar{P}_h(\mu = 0) = \frac{P_h}{2\sqrt{EIw}} = \sqrt{\frac{2}{\Delta r}}. \quad (8)$$

The second theory (solid line in Fig. 3(a), (b)) does assume lateral friction between the rod and the pipe, and adds amplification factors ψ_c^s and ψ_c^h to Eqs. (7) and (8), respectively, that include the coefficient of dynamic friction,

μ_d [19,20]:

$$\psi_c^s = \frac{q^2}{2} (1 - 1.5a^2) + \frac{1}{2q^2} \left(1 + \frac{a^2}{8} + \frac{8\mu_d}{\pi a} \right), \quad (9)$$

$$\psi_c^h = \frac{6}{3 - \pi\mu_d} \left(\frac{(\pi + 2\mu_d)(5 - \pi\mu_d)}{10\pi} \right)^{1/4}, \quad (10)$$

where $q = 1 + 0.193\mu_d^{2/3}$ and $a = 0.774\mu_d^{1/3} - 0.371\mu_d$. For our measured value of $\mu_d = 0.30 \pm 0.03$ and pinned-pinned boundary conditions, $\psi_c^s = 1.67$ and $\psi_c^h = 2.44$. In Fig. 3(a), (b) we plot (solid lines):

$$\bar{P}_s(\mu = \mu_d) = \frac{P_s}{2\sqrt{EI}w} = \frac{\psi_c^s}{\sqrt{\Delta r}}, \quad (11)$$

$$\bar{P}_h(\mu = \mu_d) = \frac{P_h}{2\sqrt{EI}w} = \frac{\psi_c^h}{\sqrt{\Delta r}}. \quad (12)$$

The two experimental datasets ($d = \{1.14, 1.6\}$ mm) collapse onto a single curve, for both \bar{P}_s and \bar{P}_h , which supports the chosen normalization. For large values of the radial clearances, these experimental results for \bar{P}_s and \bar{P}_h agree particularly well with Eqs. (11) and (12), which both included frictional interaction. For the tighter clearances, however, there is a pronounced disagreement and the frictional theory significantly overpredicts the experimental data ($\sim 50\%$ for \bar{P}_s and $\sim 100\%$ for \bar{P}_h). Simulation data for perfectly straight clearances show a similar collapse, and agree well with Eqs. (11) and (12) over all clearances, with critical forces slightly higher than those predicted. On the other hand, when geometric imperfections of the constraint are included in the simulations (to match the experiments), significant discrepancies with the predictions are found, similarly to the experimental results. The role of the geometrical imperfections of the setup in affecting the mechanical response of our system will be discussed in more detail, below, in Section 4.3.

4.3. Effect of imperfections

As described in Section 2, the acrylic pipe used in our experimental apparatus was mounted horizontally to a rigid aluminum frame at discrete points set 75 cm apart (see Fig. 1). These unsupported segments can sag under their own weight. Assuming clamped–clamped boundary conditions, the maximum deflection due to self-weight at the mid-span is [41]

$$\zeta_{\max} = \frac{wL^2}{384EI} \quad (13)$$

where L is the unsupported length of the pipe between clamps, $w = 1195 \text{ kg/m}^3$ is weight per unit length of the glass pipe, $E = 2.2 \text{ GPa}$ is its Young's modulus and $I = \pi/64(D_o^4 - D_i^4)$ is the area moment of inertia of the pipe (which we vary for pipes with different outer and inner diameters, D_o and D_i , respectively). For convenience, we define the dimensionless maximum deflection, $\eta = \zeta_{\max}/\Delta r$ such that $\eta = 0$ corresponds to the pipe being perfectly straight and $\eta > 1$ to a deflection that is larger than the radial clearance. In Fig. 4, we plot η versus Δr for all the acrylic pipes used in our experiments, and for

the two cases of $d = \{1.15, 1.6\}$ mm. Note that $\eta \gtrsim 1$ for the two tightest clearances, the third tightest clearance has $\eta \approx 0.4$ and $\eta \leq 0.05$ for $\Delta r \gtrsim 4$ mm.

We revisit the critical buckling loads plotted in Fig. 3(a), (b) that showed disagreement between experimental results and frictional theory at lower clearances, which we now understand as having larger values of η . As noted, across the whole range of Δr , simulations for a straight constraint follow Eq. (12), whereas the simulations with a geometrically imperfect pipe follow the experiments more closely.

We further evaluate the deviations of the experimental and simulated (including sag) data from Eq. (12) by quantifying the following normalized differences between the theoretical prediction with friction from Eqs. (11) and (12), $[P_s]_{th}$ and $[P_h]_{th}$, and the observed experimental and simulated results, $[P_s]_{obs}$ and $[P_h]_{obs}$, for the critical buckling loads for the onset of the sinusoidal and buckling configuration, respectively,

$$\chi^s \equiv \frac{[P_s]_{th} - [P_s]_{obs}}{[P_s]_{obs}}, \quad (14)$$

$$\chi^h \equiv \frac{[P_h]_{th} - [P_h]_{obs}}{[P_h]_{obs}}. \quad (15)$$

These can be regarded as *knockdown factors*, as often referred to in buckling analysis, with $\chi = 0$ indicating perfect agreement between experiments and theory.

In Fig. 5(a) and (b), we present χ^s and χ^h versus η , for the two rods with $d = \{1.14, 1.6\}$ mm. As discussed in Section 4.2, the simulations do not exhibit the same degree of reduction in critical loads at small clearances (large η) as in the experiments; there is significant scatter in the simulation results of Fig. 5(a) and (b). For the experimental results, however, the knockdown factor is approximately linear with imperfection size. Negative values of $\chi^{s,h}$ correspond to observed measurements greater than theoretical predictions. It is interesting to note that for the case of χ^h , there is a threshold of $\eta \sim 0.4$, below which the system is insensitive to imperfections. This indicates that there is a range, $0 < \eta \lesssim 0.4$, over which the system is tolerant to the size of the imperfections on the constraining geometry, where the idealized frictional theory [19] mentioned above is applicable. Beyond this range, however, reductions in the critical conditions for the onset of helical buckling can be significant, by as much as 300% (see Fig. 5).

5. Conclusions

We have studied the problem of buckling of a cylindrically constrained rod under compression, through a combination of precision model experiments and simulations, finding good agreement between the two, with no fitting physical parameters. These results were also compared to existing theoretical predictions that describe the data well for the larger radial clearances, but significant discrepancies were found for tighter clearances. Exploring these differences led to the recognition of the nontrivial role of geometric imperfections of the horizontal constraint, notably the sag that was present in the unsupported spans of the smaller-diameter pipes. We found that the

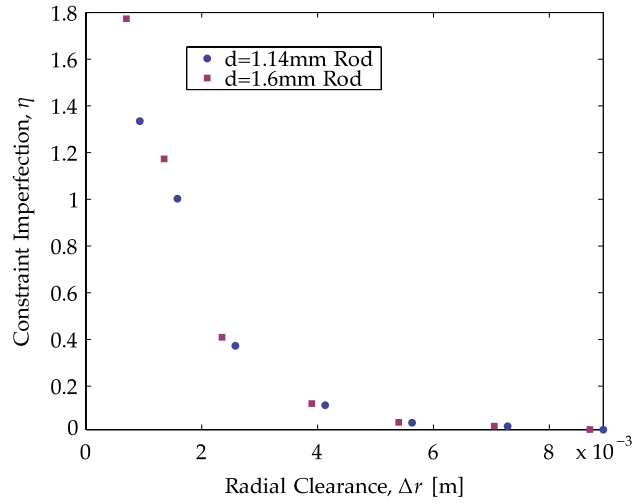


Fig. 4. Normalized maximum sag in the constraint, η , as a function of the radial clearance, Δr , for all the experimental runs.

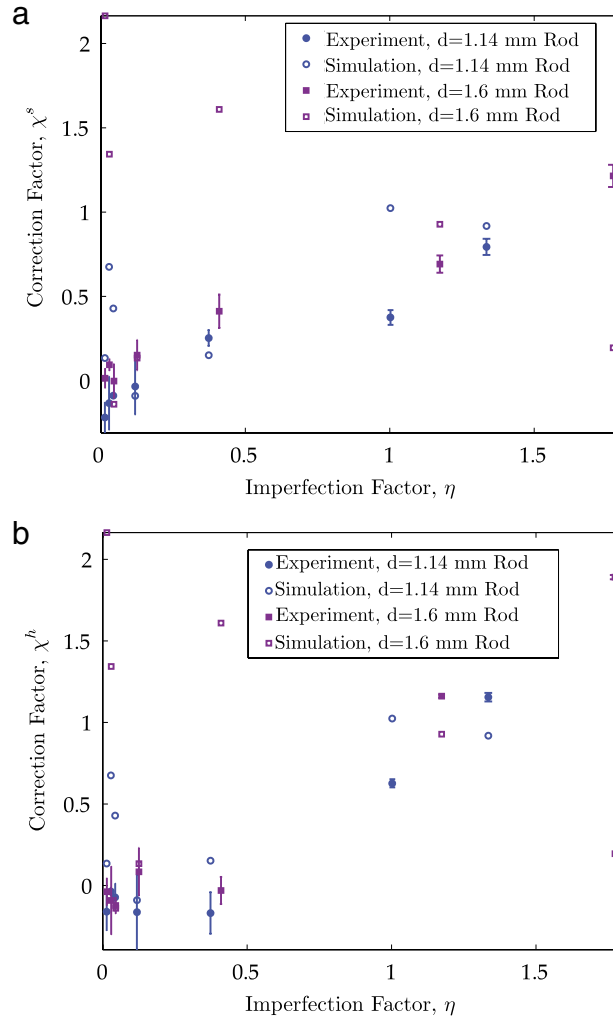


Fig. 5. Experimental deviation from theoretical prediction for critical (a) sinusoidal and (b) helical buckling load (χ^s and χ^h , respectively) as a function of constraint imperfection size, η . We note an approximately linear relationship between χ^s and η in (a), but an apparent critical value of η ($0.4 < \eta_c < 1$) in (b) below which χ^h remains relatively unaffected.

knockdown factor that reconciles our results with existing theory increased with the size of the imperfection (compared to the radial clearance). For the onset of the helical configuration, however, there was a critical threshold below which the system is insensitive to imperfections. This finding should be particularly relevant for coiled-tubing operations in horizontal wellbores with an intrinsic tortuosity, where there is a timely need to extend reach [42]. To the best of our knowledge, the importance of this knockdown (and the existence of a threshold) has not previously been reported in the literature for the context of coiled-tubing operations. Future work should focus on exploring this imperfection-dependence for different wavelengths of imperfection size, as well as imperfections not aligned with the direction of gravity. The prominence of geometry in this problem (instead of material effects) in dictating the nonlinear behavior of cylindrically constrained rods allows for the same mechanical framework to be relevant to both the benchtop and oilfield scales. However, a detailed scaling analysis that quantitatively establishes a bridge between the lab and the field scales is yet to be developed and we believe that this is another important direction for future work.

Acknowledgments

We thank Liz Dussan for helpful discussions and are grateful for financial support from both Schlumberger and the National Science Foundation (CMMI-1129894).

References

- [1] W. Klug, M. Feldmann, M. Ortiz, *Comput. Mech.* 35 (2005) 146–152.
- [2] F. Xu, W. Lu, Y. Zhu, *ACS Nano* 5 (2010) 672–678.
- [3] D. Svenšek, R. Podgornik, *Phys. Rev. E* 77 (2008) 031808.
- [4] M. Jawed, F. Da, J. Joo, E. Grinspun, P. Reis, *Proc. Natl. Acad. Sci. USA* 111 (2014) 14663–14668.
- [5] M.K. Jawed, P.M. Reis, *Extrem. Mech. Lett.* 1 (2014) 76–82.
- [6] J.L. Silverberg, R.D. Noar, M.S. Packer, M.J. Harrison, C.L. Henley, I. Cohen, S.J. Gerbode, *Proc. Natl. Acad. Sci.* 109 (2012) 16794–16799.
- [7] A. Lubinski, W. Althouse, *J. Petrol. Technol.* 14 (1962) 655–670.
- [8] P. Paslay, D. Bogy, *J. Appl. Mech.* 31 (1964) 605–610.
- [9] A. Lubinski, H. Woods, *Drilling and Production Practice*, 1953, pp. 222–250.
- [10] R. Dawson, P. Paslay, *J. Petrol. Technol.* 36 (1984) 1734–1738.
- [11] Y. Chen, Y. Lin, J. Cheatham, *J. Petrol. Technol.* 42 (1990) 140–141.
- [12] G. Deli, F. Liu, B. Xu, in: *SPE International Oil and Gas Conference and Exhibition in China*, pp. 517–523.
- [13] J. Wu, H. Juvkam-Wold, in: *SPE Production Operations Symposium*, pp. 867–876.
- [14] S. Miska, J. Cunha, in: *SPE Production Operations Symposium*, pp. 173–180.
- [15] S. Miska, W. Qiu, L. Volk, J. Cunha, in: *International Conference on Horizontal Well Technology*, pp. 207–214.
- [16] R. Mitchell, *SPE Drill. Eng.* 1 (1986) 457–465.
- [17] J.T. Miller, *Mechanical behavior of elastic rods under constraint* (Ph.D. thesis), Massachusetts Institute of Technology, 2014.
- [18] W. Qiu, in: *SPE Eastern Regional Meeting*, pp. 329–342.
- [19] G. Gao, S. Miska, *SPE J.* 14 (2009) 782–796.
- [20] G. Gao, S. Miska, *SPE J.* 15 (2010) 1104–1118.
- [21] J.-S. Chen, H.-C. Li, *J. Appl. Mech.* 78 (2011).
- [22] J. Fang, S.-Y. Li, J.-S. Chen, *Acta Mech.* 224 (2013) 2635–2647.
- [23] S.-Y. Li, J.-S. Chen, *Eur. J. Mech. A Solids* 44 (2014) 61–74.
- [24] X. He, A. Kyllingstad, *SPE Drill. Complet.* 10 (1995) 10–15.
- [25] E. Kuru, A. Martinez, S. Miska, W. Qiu, in: *SPE/IADC Drilling Conference*, pp. 1–9.
- [26] R. McCann, P. Suryanarayana, in: *Offshore Technology Conference*, pp. 511–521.
- [27] P. Suryanarayana, R. McCann, in: *Presentation given at the ASME Energy-Source Technology Conference and Exhibition, New Orleans*, pp. 23–27.
- [28] A. Martinez, S. Miska, E. Kuru, J. Sorem, *J. Energy Resour.- ASME* 122 (2000) 123–128.
- [29] G. Kirchhoff, *J. Reine Angew. Math.* 56 (1859) 285–313.
- [30] A. Love, *A Treatise on the Mathematical Theory of Elasticity*, first ed., Cambridge University Press, 1892.
- [31] A. Clebsch, *Theorie der Elasticitat Fester Korper*, BG Teubner, 1862.
- [32] J.H. Maddocks, *Arch. Ration. Mech. Anal.* 85 (1984) 311–354.
- [33] S.S. Antman, *Nonlinear Problems of Elasticity*, Vol. 107, Springer, 2005.
- [34] B. Audoly, Y. Pomeau, *Elasticity and Geometry: from Hair Curls to the Non-Linear Response of Shells*, Oxford University Press, Oxford, New York, 2010.
- [35] R.J. Roark, W.C. Young, *Formulas for Stress and Strain*, McGraw-Hill, 1975.
- [36] J. Pabon, N. Wicks, Y. Chang, R. Harmer, *Non-Linear Dynam. Deep Drill. Syst.* (2009) 83.
- [37] J.A. Pabon, N. Wicks, Y. Chang, B. Dow, R.J. Harmer, et al. *SPE Deepwater Drilling and Completions Conference*, Society of Petroleum Engineers, 2010, pp. 293–307.
- [38] J. Pabon, N. Wicks, Y. Chang, C. Chapman, V. Singh, *Modeling the transient behavior of bha/drill string while drilling*, Patent (2011) URL: <http://www.freepatentsonline.com/8014987.html>.
- [39] H.M. Hilber, T.J. Hughes, *Earthq. Eng. Struct. Dyn.* 6 (1978) 99–117.
- [40] A. Goriely, M. Tabor, *Phys. Rev. Lett.* 80 (1998) 1564–1567.
- [41] S. Timoshenko, J. Gere, *Theory of Elasticity Stability*, second ed., Dover, 1961.
- [42] J. Miller, C.G. Mulcahy, J. Pabon, N. Wicks, P.M. Reis, *J. Appl. Mech.* 82 (2015) 021003.